A Comparative Study of Direct and Graphite-Mediated Oxidation of Large PAHs

Jürgen Weippert,[†,‡] Philipp Huber,[†] Jakob Hauns,[†] Akimitsu Narita,[¶] Klaus Müllen,[§] Konstantin Y. Amsharov,[∥] Artur Böttcher,[*,†] and Manfred M. Kappes[†,⊥]

[†]Institute of Physical Chemistry, KIT, 76131 Karlsruhe, Germany

[‡]Fraunhofer IAF, Fraunhofer Institute for Applied Solid State Physics, 79108 Freiburg, Germany

[¶]Okinawa Institute of Science and Technology Graduate University, 904-0495 Okinawa, Japan

[§]Max Planck Institute for Polymer Research, 55128 Mainz, Germany

[∥]Institute of Chemistry, Martin-Luther-Universität Halle-Wittenberg, 06120 Halle, Germany

[⊥]Institute of Nanotechnology, KIT, 76344 Eggenstein-Leopoldshafen, Germany

E-mail: artur.boettcher@kit.edu

Abstract

We have used a surface-science based, ion-beam-soft-landing approach to study the heterogeneous oxidation of a series of large polycylclic aromatic hydrocarbons (PAHs) deposited onto highly oriented pyrolytic graphite (HOPG). The reactivities of well-defined thin films of hexabenzocoronene ($C_{42}H_{18}$), pentacene ($C_{22}H_{14}$), the Fullerene Precursor ($C_{60}H_{30}$) and rubrene ($C_{42}H_{28}$) with effusive beams of oxygen atoms were compared to the reaction outcome upon depositing a monolayer of the same PAHs onto a preoxidized graphite surface. In both cases, sublimable oxidized derivatives of PAHs were observed using mass-resolved temperature programmed desorption (with compositions assigned using oxygen isotope labelling where necessary). For all PAHs investigated, the on-top oxidation of multilayers leads to epoxides. By contrast, the products of the oxidation of (sub)monolayers are seen to depend on the molecular structure of the PAH. While the flatly adsorbing planar PAHs react to form lactones and quinones, the highly nonplanar rubrene does not show analogous surface-mediated chemistry, instead forming epoxides exclusively. These observations when taken together with our previous study of coronene oxidation are of potential interest for sp^2-nanocarbon-based oxidation catalysis. Furthermore, we have demonstrated a UHV-based route to sublimable oxides ranging in size up to $C_{60}H_{30}O_5$ which may be useful for nanotechnological applications.

Introduction

Over the last 15 years the rise of graphene and the resulting intense interest in graphene-based nanodevices has led to a new slant on the heterogeneous reactions of PAHs. PAHs can be regarded as atomically precise pieces of nanographene (of uniform size).[1] They have been interconnected on surfaces to form "engineered" nanographene topographies with useful size- and structure-dependent electronic properties.[2] There is an analogous but still untrodden path between oxidized PAHs, oxidized nanographene and graphene oxides (GO).

GOs are known to have a range of useful properties which complement those of graphene.

Among them, GOs show photoluminescence[3] which can potentially be employed for optoelectronic devices,[4] if better control of the size and functionalization degree could be achieved. A major issue in the synthesis is that the classical methods to generate GOs, like the Hummers-Offeman[5] or the Staudenmaier[6] method, involve the use of harsh oxidizing acids which do not lead to well-defined nanostructures but instead to a broad distribution of GO sheet sizes and oxide functionalities as described by the Lerf-Klinowski model.[7] New preparation methods for graphene oxides (GOs) are therefore currently of great interest.[8–12] Polycyclic aromatic hydrocarbons (PAH) are comparatively inert and therefore difficult to functionalize precisely with oxygen under normal wet chemical synthesis conditions. An overview over the results of wet and photochemical oxidation procedures can be found below in the "known PAH oxides" section. A controlled oxidation of large PAHs sublimed onto well-defined surfaces offers one possible approach to achieve atomically precise oxidized nanographene.

Towards this end we became interested in the heterogeneous oxidation of HOPG-surface-bound PAHs using near-thermal energy atomic oxygen. While there are studies regarding the reaction between PAHs and atomic oxygen,[13–15] especially with astrochemical interest, these typically focused on etching processes and not on the direct molecular oxidation products. We have recently probed the oxidation of thin coronene ($C_{24}H_{12}$) films using mass-resolved temperature programmed desorption (TPD) to characterize the volatile oxidic products generated with these conditions.[16,17] Interestingly, we observed significant amounts of intactly desorbing coronene oxides.

We found that the distribution of these desorbable oxidic products depended strongly on the oxidation procedure. Three different procedures (1.-3.) were applied all making use of oxygen atoms as schematically depicted in fig. 1.

1. A thick multilayer coronene film was deposited onto the basal plane of HOPG and subsequently treated with a perpendicularly incident, near-thermal energy effusive beam of oxygen atoms from a plasma source.[16] This led to intactly desorbable coronene epoxides and, for higher oxidation degrees, eventually coronene ethers - as assigned by
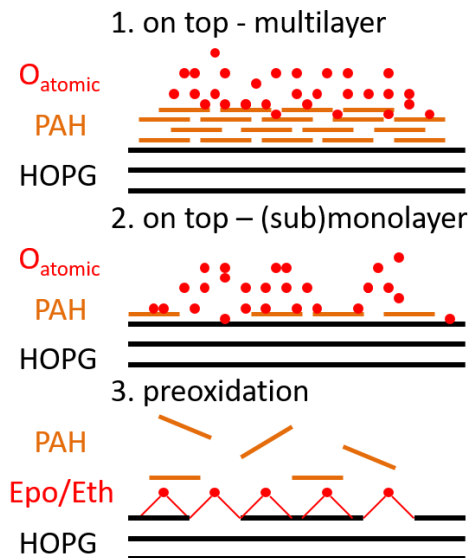
3

Figure 1: The three different O-atom based oxidation procedures applied to all PAHs studied here: 1. Deposition of several PAH layers is followed by on top-oxidation with an effusive beam of near-thermal atomic oxygen; 2. The same sequence as in 1. but now with a PAH (sub)monolayer and 3. PAH oxidation by deposition of (sub)monolayer coverages onto a preoxidized HOPG surface prepared by treatment with O-atoms (predominantly contains graphene epoxides and some ethers).

combining mass-resolved temperature programmed desorption (TPD) with X-ray photoelectron spectroscopy (XPS) and density functional theory (DFT) calculations. We rationalized this reaction outcome as being analogous to the O-atom functionalization of the HOPG[18,19] basal plane which also showed epoxides as the major products at low exposures while ethers appeared for higher oxygen atom loads. Formation of ethers on HOPG is thought to reflect a concerted unzipping mechanism[20] which opens the C-C bond underneath an epoxy unit if a second oxygen atom adsorbs nearby thus forming e.g. oxepine or dioxepine units.

2. Interestingly, (sub)monolayers of coronene, also treated with O-atoms in the same way, reacted to fundamentally different products than the thick films.[17] Based on oxygen isotope labelling experiments we were able to assign these products as lactones (predominantly 2H-Benzo[6,7]perylo[1,12-bca]pyran-2-one) and quinones (most likely 1,2-Coronendione).

4

3. In the third coronene oxidation procedure we made use of preoxidized HOPG, i.e. a graphite surface covered by epoxides and, for higher oxygen doses, some ether functional groups. Coronene was deposited onto this oxide layer and reaction products were again probed by mass-resolved TPD. This yielded the same products as observed for procedure (2.) but with higher yields. Additionally, a minor oxidation product most likely containing a cyclopentadienone ($1H$-benzo[ghi]cyclopenta[pqr]perylen-1-one) unit was detected. Furthermore, TPD uncovered a new, weakly binding state of coronene which was assigned to unreacted coronene localized atop the epoxide layer in addition to the coronene state bound more strongly to unfunctionalized HOPG.

The lactone and quinone products of submonolayer reaction procedures (2.) and (3.) clearly demonstrate that the HOPG surface can act as a catalyst or at least as a mediator for coronene oxidation. In recent years sp^2 carbon materials have successfully been used for several catalytic processes such as desulfurization,[21] dehydrogenation[22] or Baeyer-Villiger oxidation.[23] In particular the latter process is of interest for our coronene study since the product of this reaction is a lactone as well.

In order to determine whether such surface-mediated oxidation products are specific only to coronene, we followed the same oxidation protocol with thin films of four additional, structurally different PAHs (see figure 2): (i) hexa-*peri*-hexabenzocoronene (HBC), (ii) pentacene, (iii) the Fullerene Precursor[24] (FPC) and (iv) rubrene (Rub). We find a correlation between the PAHs' molecular structure type and the composition of the oxides resulting from all three different oxidation procedures.

Background

General properties of the investigated molecules

The choice of the investigated PAHs has been made to cover a broad structural variety of disk-type systems. The D_{6h}-symmetric HBC and the D_{2h}-symmetric pentacene represent
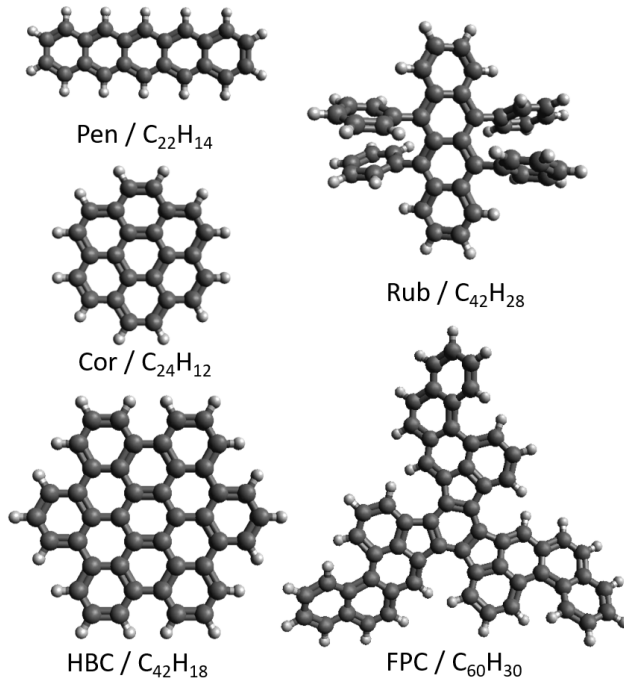
Figure 2: Schematic molecular structures of pentacene (Pen, $C_{22}H_{14}$), coronene (Cor, $C_{24}H_{12}$), hexabenzocoronene (HBC; $C_{42}H_{18}$), rubrene (Rub, $C_{42}H_{28}$) and the Fullerene Precursor (FPC; $C_{60}H_{30}$).

borderline cases since the former is chemically extremely stable while the latter is not. This has already been explained by the famous Clar rule:[25–28] HBC can be electronically described as being made up of seven aromatic sextets as opposed to pentacene which possesses only one such sextet as depicted in fig. 3. HBC, like coronene itself, and pentacene are planar. Rubrene is special since it carries strongly twisted phenyl substituents which also impose some non-planarity of the tetracene core. Finally, the fullerene precursor FPC with 60 carbon atoms stands out by comprising three fused five-membered rings which also causes some bending of the disc structure.

 The optical bandgaps[29–33] (see table in the supplement) range from 1.85 eV for pentacene to 3.29 eV for coronene whereby large gaps generally correspond to high chemical stability. Theoretical HOMO-LUMO gaps from our own calculations reproduce this trend.
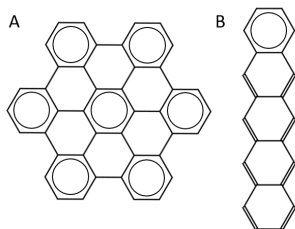
Figure 3: Structural formulae of A: HBC with seven Clar sextets and B: pentacene with only one Clar sextet

Known PAH oxides

Multiply oxidized coronene derivatives have been accessed synthetically. Quinones have for example been made under appropriately stringent volume phase reaction conditions.[34,35] Several additional oxidic derivatives of coronene have also been synthesized including coronene tetracarboxylic acid anhydride,[36] methoxy-substituted coronene[37] and tri- to octacarboxy-substituted coronenes.[38] All of these have the same intact coronene skeleton but terminating functionalities which differ significantly from the unprecedented rim-epoxy derivatives, which we found upon treating thick coronene films to thermal energy oxygen atoms at the solid-gas interface.[16]
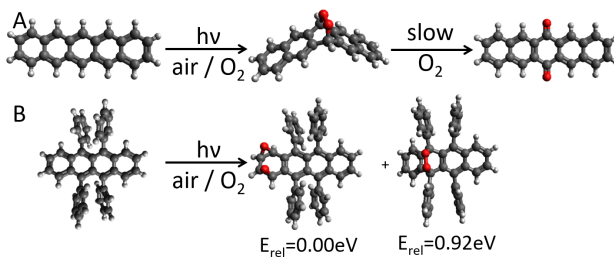

Figure 4: A: Photochemical oxidation of pentacene under ambient conditions generates an endoperoxide intermediate which slowly gets autoxidized to a quinone.[39] B: Photochemical oxidation of rubrene in air is thought to form a double epoxide and an endoperoxide.[40,41] The latter is less stable than the former on the basis of our DFT calculations.

Similarly, only a limited number of oxidized derivatives of the PAHs studied here have previously been accessed in condensed phase synthesis. A symmetric alkoxy derivative of HBC has been reported[42] based on the assembly of alkoxy-substituted precursors. However, to

the best of our knowledge HBC-epoxides, -lactones and -quinones have not yet been made in bulk. For FPC, there have been no literature reports of oxides that we are aware of.

Both small-bandgap PAHs that also have singular Clar sextets in this study can be oxidized photochemically: Pentacene forms an endoperoxide when exposed to light under ambient conditions.[39] This process is followed by slow autoxidation to form 6,13-pentacenequinone. This quinone can also be formed by oxidizing pentacene with chromic acid[43] or by aldol condensation of ortho-phthalaldehyde with cyclohexanedione.[44] Pentacenequinones and analogous fully conjugated tetrones have been studied with regard to organic solar cells[45] formation of self-assembled monolayers[46] and for electrocatalytic applications.[47,48] (Sublimable) pentacene epoxides and lactones appear to be reported here for the first time. Rubrene is even more photosensitive than pentacene and is thought to be photochemically oxidized to epoxides and endoperoxides[40,41,49] under ambient conditions (on the basis of spectroscopic studies of corresponding thin films).

Experimental and computational methods

Sample preparation

Pentacene (Fluka, 99.7%) and rubrene (Acros, 99%) were obtained from commercial sources. HBC was synthesized as described by us in the literature.[50] FPC was synthesized according to a previous procedure.[51]

All thin film samples were prepared by mass-selective ion beam soft-landing with the same UHV setup used for the coronene studies.[16,17] Briefly, the desired PAH was sublimed from a Knudsen effusion cell and subsequently ionized by electron impact ($E_{el} \approx 70$ eV). The resulting mixed molecular beam was split into anions, neutral molecules and cations using an electrostatic deflector. The cations were then mass-selected by a quadrupole mass filter (Extrel Merlin, 1-4000 u) and directed at a clean HOPG substrate (SPI supplies, SPI-2 grade) held at a retarding potential which ensured fragmentation-free soft landing ($E_{incident} \approx 6$ eV).

The deposited ion current was measured with a picoamperemeter (Keithley); its integral, i.e. the ion dose, was converted into monolayers (ML) using conversion factors as determined in our previous work[52,53] (see section on quantifying coverages and compact table 2 in the Supplementary Information).

Ion beam deposition has the advantage that impurities present in the starting material (and differing significantly in mass from the PAH in question) can be quantitatively removed and the deposited amount of material can be controlled with deviations $< 1\%$. The resulting spot has a diameter of ca. 2.5 mm and a rim-to-middle height difference of ca. 20%. However, there is a trade-off between mass resolution and acceptable ion current such that typically a small fraction of the ions transmitted to the surface comprised partially dehydrogenated fragment species in addition to the abundant parent ions. In our previous studies of coronene (see supplements[16,17]) we therefore compared thin films prepared by deposition of ions to films generated by direct Knudsen effusion of neutrals - to ensure that the oxidation outcome is not affected by small amounts of dehydrogenation associated with ionization. The supplement of this paper contains an analogous comparison for soft-ionized pentacene yielding the same conclusion, i.e. no effect of dehydrogenated fragments on oxidation outcome. The other three PAHs studied here are assumed to behave analogously.

Oxidation was performed using a microwave plasma source[54] (Tectra Gen II, copper induction rod) equipped with (i) a leak valve through which we dosed alternately $^{16}O_2$ (Messer Griesheim, 99.9998%) or if desired $^{18}O_2$ (Linde, 99.9998%) and (ii) an electrostatic deflection plate to prevent charged species from striking the sample. The typical settings yielded a chamber pressure of $1 \cdot 10^{-5}$ mbar which corresponded to an O-atom flux at the target of $1.5 \cdot 10^{13}$ $Os^{-1}cm^{-2}$ (calibration by residual gas analyzer). At these settings there is no significant contribution from molecular or atomic oxygen in excited electronic states.[16,55,56] Due to the photochemical activity of pentacene and rubrene we shielded the sample from external light sources to the greatest extent possible - except for scattered light from the plasma source itself.

Temperature programmed desorption and assignments

After reaction with O-atoms, all thin film PAH samples were characterized by Temperature Programmed Desorption Spectroscopy (TPD). For this, HOPG substrates covered with the (oxidized) PAH of interest were heated with a linear heating rate β (FHI ELAB-GO74 heating ramp generator). Molecules desorbing in a characteristic temperature range were monitored by a quadrupole mass spectrometer (Extrel Merlin, 1-4000 u, electron impact ionization). The resulting mass-resolved desorption spectra allow for the determination of the binding energies of both unreacted parents and specific oxidized products by a Redhead analysis[57] if the frequency factor ν of the desorption is known. With the heating rate variation method[58] we had previously determined the frequency factors of HBC[52] as $2.9 \cdot 10^{17 \pm 1.3}$ Hz, of pentacene[52] as $2.6 \cdot 10^{16 \pm 1.5}$ Hz and of FPC[53] as $7.0 \cdot 10^{16 \pm 0.6}$ Hz, respectively for desorption from HOPG. In the former study this method could not be applied to rubrene due to methodological constraints regarding lateral interactions.[53] Instead, we assumed that the HBC frequency factor could also be applied to rubrene as both consist of 42 carbon atoms (our investigations showed a correlation between molecular size and frequency factor[52]). Here, we will assume that PAH-oxide frequency factors correspond closely to those of the respective unoxidized PAH.

Our setup allows to rapidly acquire multiple mass spectra during the desorption ramp. These can be converted into temperature resolved mass spectral maps (TRMS) which provide contour plots of ion intensity versus mass and temperature. Assuming negligible ionization induced fragmentation of desorbing neutral species, TRMS maps allow for the direct correlation of surface processes and corresponding reaction products.

To facilitate the composition determination of reaction products we generally compared TRMS maps after oxidation with ^{16}O versus ^{18}O - under otherwise identical conditions. For this, mass shifts of oxides relative to the unoxidized PAHs were determined by integrating the corresponding TRMS maps along the desired segment of the temperature axis and fitting the resulting mass spectrum with a set of Gaussian functions. Detailed examples of this

procedure can be found in our previous work on coronene.[16,17] In the latter study $^{16}O/^{18}O$ labelling allowed us to identify epoxides, ethers, lactones and quinones as the major reaction products of coronene with atomic oxygen (for a depiction of the corresponding molecular structures see fig. 5). Up to 7 oxygen atoms were observed to be sequentially added – with addition sometimes also associated with loss of CO and H_2.

In the following we will encounter analogous epoxide, ether, lactone and quinone oxidation products, sometimes in combination. It is therefore useful at this stage to introduce a general nomenclature for PAH oxidation products which allows to assign specific desorption signals in TRMS maps to product classes in a compact notation (see also fig. 5).

- The initial PAH monolayer desorption peak will be **0** or **a** depending on the following oxides.

- Desorption signals assigned to epoxides are denoted by the number n of oxygen atoms which have been taken up by the PAH. For oxygen uptakes approaching the bulk graphene limit of one epoxy unit per hexagon the aforementioned unzipping mechanism[20] is thought to take place which leads to ether functionalizations. Therefore, beyond a certain **n** (and depending on the size of the PAH) we assume a transition from epoxide to ether derivatives has occured.

- Lactones will be denoted **b**, quinones **c** and dilactones **d**.

- If a desorbing species is assigned as having two different types of oxygen-containing functional groups, the indices are put in series, e.g. **1d** would be a PAH dilactone that has additionally adopted one epoxy (or one ether) group.

- Sometimes a high- and a low-temperature desorption component are observed at the same mass-to-charge ratio. These are designated with lower-case indices $\mathbf{a}_n$, in the sequence from highest to lowest temperature.
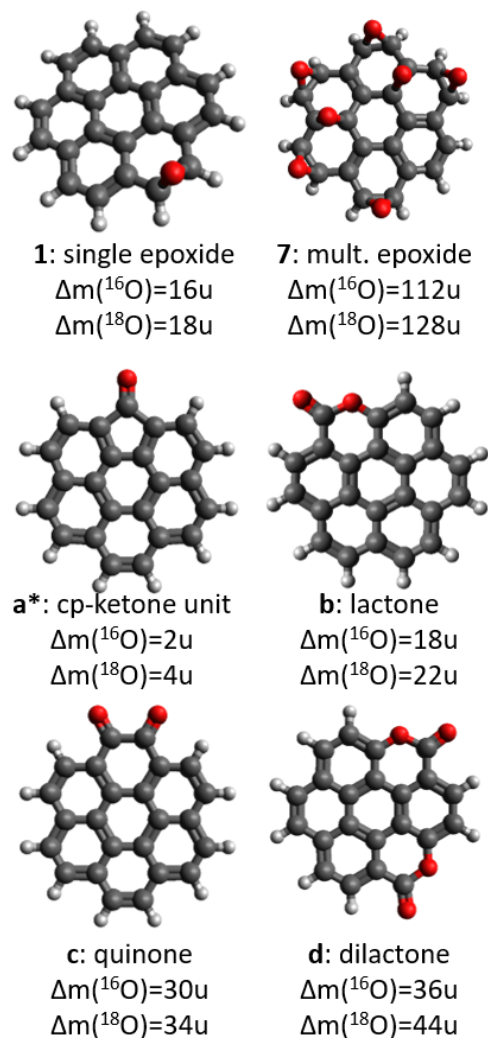
1: single epoxide
$\Delta m(^{16}O)=16u$
$\Delta m(^{18}O)=18u$

7: mult. epoxide
$\Delta m(^{16}O)=112u$
$\Delta m(^{18}O)=128u$

a*: cp-ketone unit
$\Delta m(^{16}O)=2u$
$\Delta m(^{18}O)=4u$

b: lactone
$\Delta m(^{16}O)=18u$
$\Delta m(^{18}O)=22u$

c: quinone
$\Delta m(^{16}O)=30u$
$\Delta m(^{18}O)=34u$

d: dilactone
$\Delta m(^{16}O)=36u$
$\Delta m(^{18}O)=44u$

Figure 5: Explanation of the compact notation used for assignment of mass shifts in TRMS maps after oxidation with ^{16}O and ^{18}O based on our previous work.[16,17] Numbers **n** (e.g., **1** and **7** as shown) stand for the number of epoxide (or possibly ether by unzipping the C-C bond under an epxoxide) groups chemisorbed onto the PAH carbon framework. **a*** at a mass slightly higher than that of the educt PAH possibly contains a cyclopentadienone unit ("cp-ketone" as shown) which may be an intermediate in the formation of a lactone **b** upon further oxidation. Heavier oxides can include quinones **c** and dilactones **d**. The notation is used independent of whether or not the TRMS map shows all oxides of the corresponding series, e.g. if no lactones are observed, quinones are still denoted as **c**. If two types of oxide are combined in the same product molecule, the the indices are also combined, e.g. a lactone with two epoxy groups is designated as **2b**

- **a**** represents an oxide with a mass slightly higher than that of the unoxidized PAH, e.g. with a cyclopentadienone unit.

In addition to product (mass) assignments, the TRMS maps also allow for the correlation of processes: if two species desorb at the same temperature, they may simply have similar binding energies. On the other hand, the lighter species may be a fragment of the heavier one (as induced by electron impact ionization). In our previous work we have for example used the observation of CO_2 elimination upon ionization to assign desorption of on-surface generated lactones.[17] Two species desorbing at different temperatures must definitely result from two different processes on the surface.

In the following, we will usually only show TRMS maps acquired after oxidation with ^{16}O. ^{18}O measurements (always carried out too) will only be presented if they are more suitable to demonstrate specific effects. Additionally, selected TRMS maps can also be found in the supplement.

Note further, that for better discrimination of individual mass spectral features we will present most TRMS contour plots in one of two differently-colour-coded logarithmic intensity scales - as denoted in the repective captions (see also figure 6B)::

- **NLIS**: Normal Logarithmic Intensity Scale, natural logarithmic scale from 5 (blue) to 450 (red) event counts/0.25 s

- **ELIS**: Expanded Logarithmic Intensity Scale, natural logarithmic scale from 1 (blue) to 450 (red) event counts/0.25 s

For HBC, pentacene and rubrene, we performed additional experiments to quantify the overall yield of desorbed oxides. These were determined by dividing the integrated desorption intensities of the oxides by the integrated desorption intensity of an unoxidized monolayer of the corresponding PAH and the initial coverage. Usually this leads to well-reproducible yields with deviations below 1 percentage point. However, as will be shown below, the overall FPC desorption intensities were too small to allow for a statistically significant oxide yield determination.

Computational methods

Candidate structures for PAH oxides identified on the basis of TRMS maps (and isotope labelling) were calculated by DFT using Turbomole.[59,60] We generally followed a two-step sequence: First starting geometries were manually generated and preoptimized with the BP86 functional[61,62] and a def2-SVP basis set[63] in the RI approximation.[64] In order to avoid transition states caused by bond rotation or other intramolecular rearrangements, vibrational frequencies were calculated at this level with the aoforce tool[65] implemented in Turbomole. Then final geometries were calculated making use of the B3LYP functional[61,66–68] with the def2-TZVP basis set[69] in the RI approximation.[70] In the case of rubrene, the Grimme-D3[71] correction was applied for all calculations in order to account for dispersion interactions between the outer phenyl rings.

Results and discussion

Hexa-*peri*-hexabenzocoronene, HBC

We begin by discussing the oxidation of hexabenzocoronene since it is a flat PAH like coronene and we therefore expect it to exhibit similar behaviour.

Fig. 6A shows a representative TRMS map after oxidation of an HBC multilayer (20 ML). Apart from the unreacted mono- and multilayer signal **0**, a series of peaks with mass shifts characteristic for epoxides **1-5** is observed. Note that epoxide **4** manifests a rather noisy desorption signal perhaps indicating an additional unresolved oxide of slightly different mass hidden below the $C_{42}H_{18}O_4$ desorption feature. The overall oxide yields, shown in fig. 6C, add up to ca. 8%, corresponding to 1.6 ML. This suggests, that large parts of the topmost layers have been converted into desorbable oxides as also seen for coronene.[16] The epoxide **1** ($C_{42}H_{18}O$) desorbs at ca. 600 K while **5** ($C_{42}H_{18}O_5$) desorbs at 650 K. This corresponds to a slight binding energy increase from 2.1 eV to 2.3 eV. An analogous shift with increasing
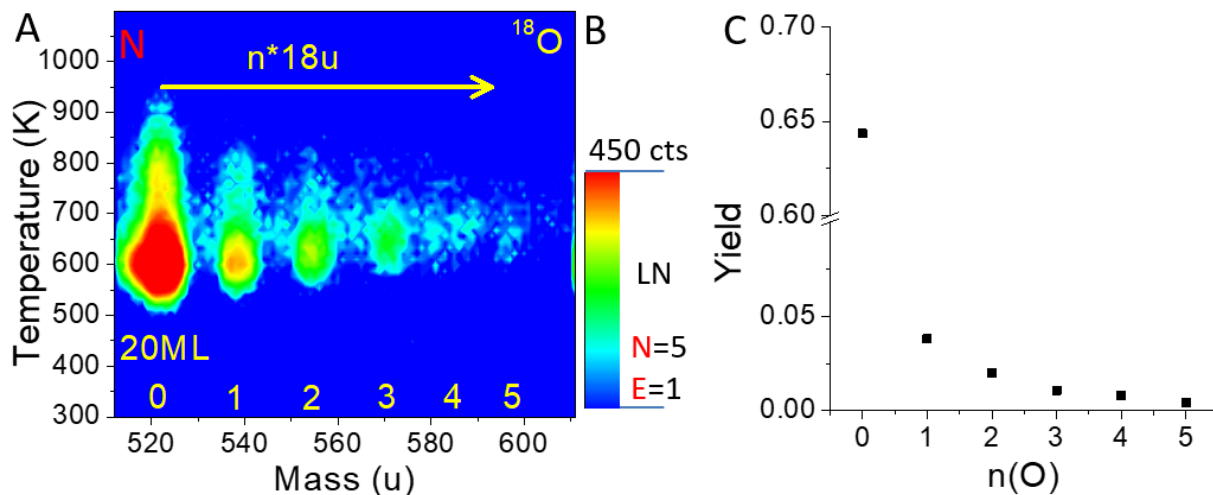
Figure 6: HBC multilayer oxidation experiments; A: TRMS map (NLIS) of an HBC oxide film generated by on top-oxidation of 20 ML HBC with ^{18}O, D_O=4.5·10^{15} cm^{-2}, β=4.3 K/s, note the series of epoxide products **1-5**; B: Yields for the oxides (for yield definition see main text)

number of adopted oxygens was observed for coronene.[16]

While the HBC multilayer oxidation outcome is quite analogous to that of thick coronene films, the on-top oxidation of an HBC monolayer (fig. 7A) still yields predominantly epoxides while the lactone **b** and dilactone **d** signals appear only as traces. Note, that the region between **3** and **4** contains some elevated noise which in analogy to the multilayer indicates the existence of an additional minor species.

A possible interpretation of this would be that the large HBC molecules shield the surface sufficiently from the impinging oxygen atoms such that the surface mediation does not take place. For HBC monolayers, all oxides desorb in the same temperature range as unreacted HBC - slightly below 750 K. Since the HOPG surface appears not to be significantly involved in the oxidation of HBC monolayers, it is not surprising that several epoxide products show desorption yields above 10% (see fig. 7B) which is significantly higher than found for coronene (sub)monolayers.[17]

In preoxidation experiments (fig. 7C) on the other hand, HBC behaves mostly like coronene. The dominant oxide is the lactone **b** and we observed traces of quinones/dilactones (**c**+**d**).
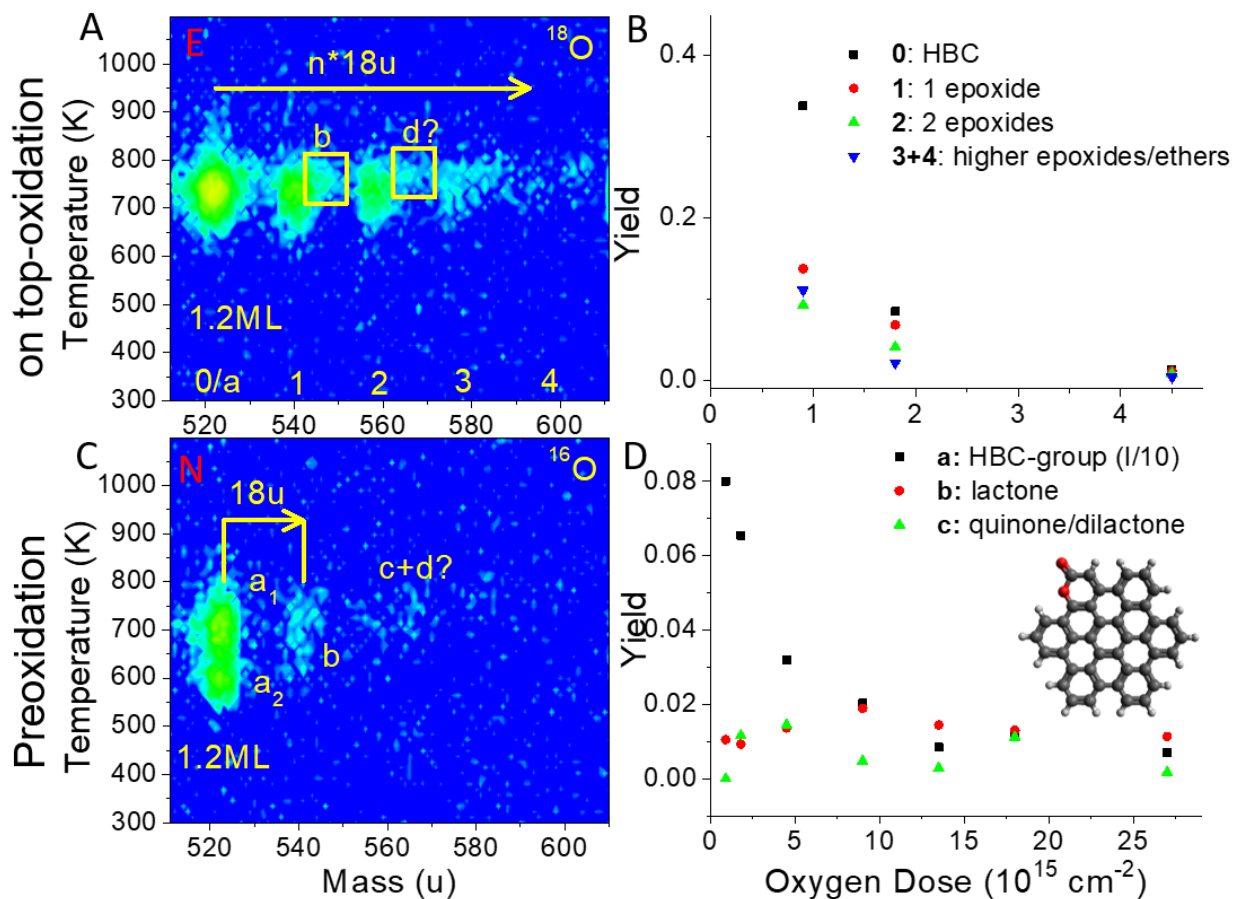
Figure 7: HBC monolayer oxidation; A: TRMS map (ELIS) of 1.2 ML HBC after oxidation with ^{18}O, D_O=0.9·10^{15} cm^{-2}, Products are still dominated by epoxides with possibly also some traces of lactones b and dilactones d visible; B: Oxide yields for all species from (A) as a function of the oxygen dose; C: TRMS map (NLIS) of 1.2 ML HBC deposited onto HOPG preoxidized with ^{16}O, D_O=4.5·10^{15} cm^{-2}, oxide products are dominated now by lactones b; D: HBC desorption and oxide yields for all species from (C) as a function of the preoxidizing oxygen dose, inset: most stable lactone structure. For both maps β=4.3 K/s.

The HBC signal a splits up into a regular component a_1 and a low-temperature component a_2 which, similar to coronene, can be interpreted as unreacted HBC sitting atop a graphene oxide surface region. The overall oxide yields are comparatively small (see fig. 7D, strong statistical fluctuations for c+d).

Pentacene

Pentacene is the second planar PAH in this study and therefore will be discussed next. Pentacene adsorbs on HOPG in a coplanar manner at small coverages but at higher coverages forms a herringbone structure with individual molcules tilted away from the surface.[72,73] For this reason, the ion dose necessary to form a saturated monolayer of pentacene is five times larger than for the similar-sized PAH coronene.[52] We therefore performed the sub-monolayer oxidation experiments at pentacene coverages for which the coplanar adsorption phase should still exist.

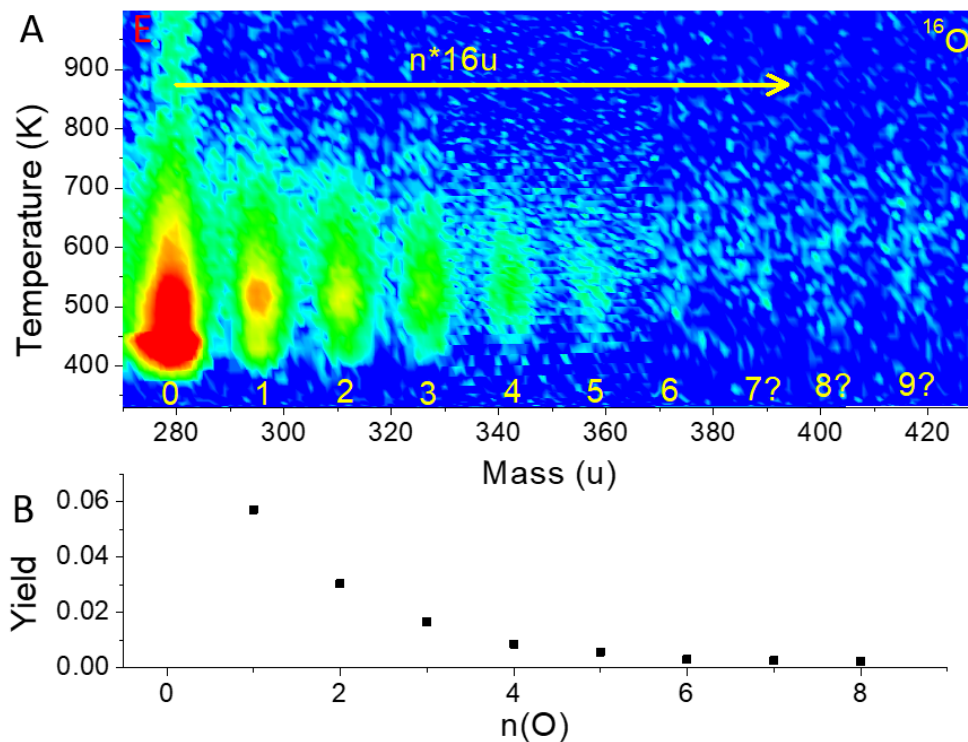The on top-oxidation of a thick pentacene film, as depicted in fig. 8A, also leads pre-

Figure 8: Pentacene multilayer oxidation; A: TRMS map (ELIS) of 5 ML pentacene after oxidation with ^{16}O, D_O=4.5·10^{15} cm^{-2}, β=4.0 K/s, showing a series of **0-9** adopted epoxy or ether functionalities; B: corresponding oxide yields (unreacted pentacene desorption: 73%)

dominantly to epoxides **1-5**. Traces of more highly oxidized species **6-9** are also observed implying that some of the oxygen atoms are bound as ethers (reflecting unzipping according to.[20] Interestingly, the oxide desorption temperatures do not lie in the range of pentacene

multilayer desorption (ca. 430 K[74]) but instead fall around 500 K (1.6-1.8 eV binding energy). The origins of this increase are uncertain, but the effect itself has already been seen in our previous work on coronene epoxides. The fact that the desorption of the unreacted pentacene multilayer has already occurred when the oxides desorb suggests that a diffusion process takes place in which the oxide molecules diffuse down to the surface before the underlying pentacene species can desorb. Alternatively, it is possible that epoxy functionalities are moved down via intermolecular oxygen atom transfer. However, we consider this less likely since such a chemical process would probably be much slower than a purely physical diffusion process. The overall oxide yield, shown in detail in fig. 8B, is about 13% at the dose used, while 73% of the deposited pentacene desorbs and 14% must have formed different products, e.g. by decomposition processes or by forming non-desorbable intermolecular adducts. 73% of initial 5 ML coverage correspond to 3.65 ML equivalents, so no oxygen atoms reached below the second highest layer.

The submonolayer experiments, represented in fig. 9A-E, depict a surprisingly diverse oxidation behaviour. On top-oxidation (fig. 9A) again generates an epoxide **1** followed by a quinone **0c**. It is unclear whether the structure of this quinone is identical to the quinone produced by photochemical oxidation[39] of pentacene, 6,13-pentacenequinone. Note, that this is also the most stable quinone based on our DFT calculations. Alternative, less stable structures are shown in the supplement. Also, oxides with combined quinone and epoxy/ether functionalities **1c**, **2c** and (possibly) **3c** are observed. Lactones **b** or **d** are completely absent. As the oxide yields (fig. 9B) show, the epoxide **1** dominates for low oxygen doses while at high doses the relative yield of quinone **0c** becomes larger than that of the epoxide. Combined oxides **nc** become slightly more pronounced (relatively) at higher doses.

The preoxidation experiments (fig. 9C) clearly show the quinone $0c_1$ as the dominant oxide formed. Note, that in contrast to on-top monolayer oxidation, the pure epoxide **1** is now absent and replaced by a lactone **b** signal. The combined oxides **1c** and **2c** are still observed. Taken together, this therefore constitutes direct evidence for the uptake of an epoxy
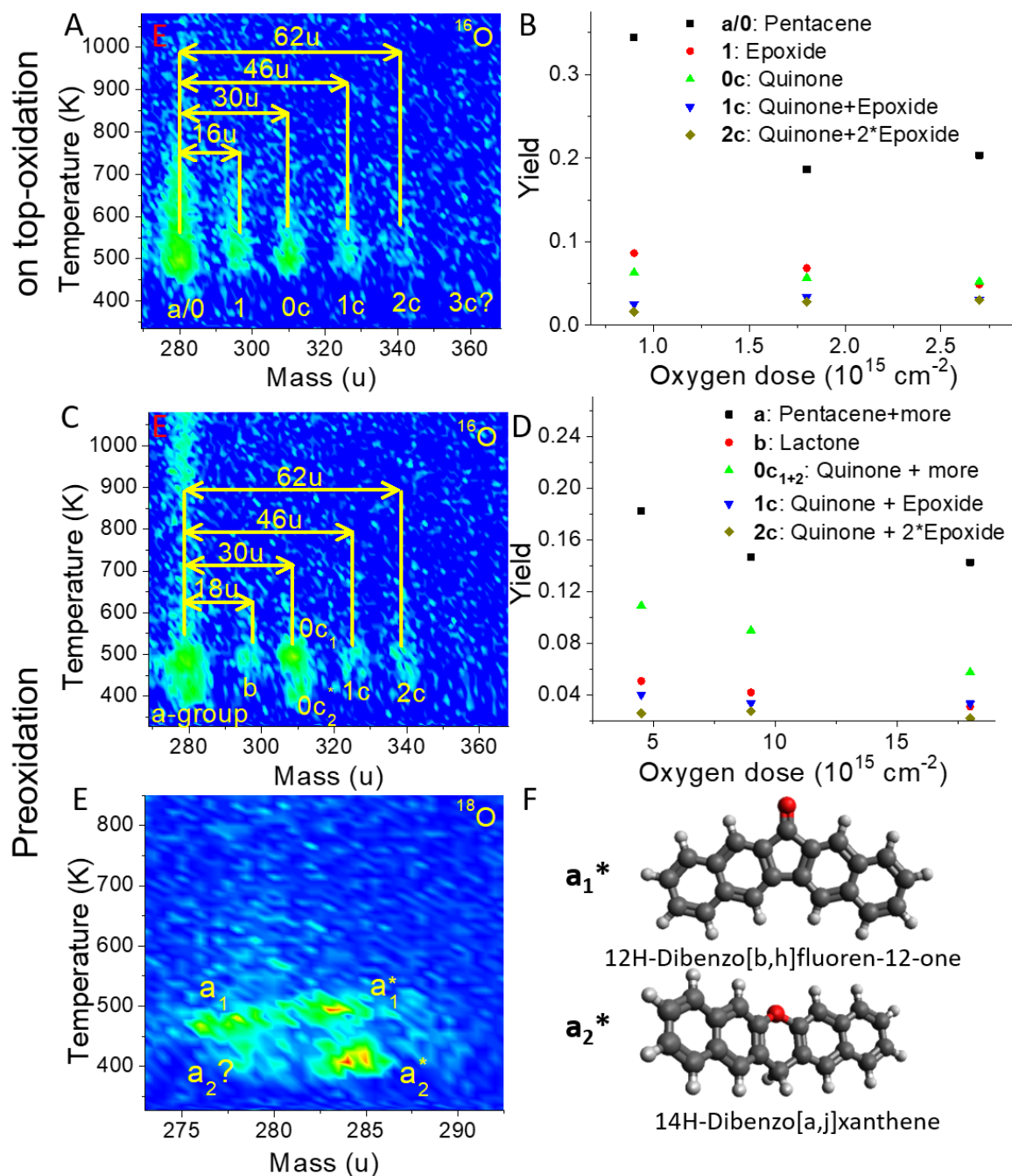
18

Figure 9: Pentacene monolayer oxidation; A: TRMS map (ELIS) of 0.33 ML pentacene after oxidation with ^{16}O, $D_O=1.8\cdot10^{15}$ cm^{-2}, showing quinones and epoxides; B: Oxide yields for all species from (A) as a function of the oxygen dose; C: TRMS map (ELIS) of 0.33 ML pentacene deposited onto HOPG preoxidized with ^{16}O, $D_O=1.8\cdot10^{15}$ cm^{-2}, showing primarily quinone $0c_1$ formation; D: Oxide yields for all species from (C) as a function of the preoxidizing oxygen dose; E: highly resolved TRMS map for a sample prepared as in (C) using ^{18}O, linear scale (0-36); F: the most stable structural candidates for the a_1^* and a_2^* peaks. For all spectra β=4.0 K/s

19

functionality from the surface leading to a unique reaction product not observed after on-top oxidation. The quinone signal $\mathbf{0c_1}$ is also associated with a weak low-temperature component which we have labelled $\mathbf{0c_2^*}$. Since it is 2 u heavier than the quinone for both oxygen isotopes, the mass would seem to fit to an endoperoxide or a double epoxide. A low-temperature oxide component like this has not been observed for any other PAH investigated by us so far. We speculate that it may be associated with the adoption of two oxygen atoms from the epoxy carpet of HOPG to form a product which is more loosely bound to the substrate than the quinone. The overall oxide yield is 23% for the lowest O-atom dose probed, $4.5 \cdot 10^{14}$ cm^{-2}, as shown in fig. 9D, and drops steadily with higher preoxidation doses. This is in contrast to coronene for which the highest oxide yields under preoxidation conditions were reached at the highest O-atom doses probed ($1.8 \cdot 10^{15}$ cm^{-2}).

Note also, that the pentacene desorption signal $\mathbf{a}$ is now itself split into three or possibly four components ("$\mathbf{a}$ group"). As fig. 9E shows, the unreacted pentacene/HOPG signal $\mathbf{a_1}$ no longer dominates the spectrum at this O-atom dose. Also, there is no clear low-temperature pentacene component $\mathbf{a_2}$ for any oxygen dose applied in contast to the clear feature a2 feature seen for HBC. Instead an oxide $\mathbf{a_1^*}$ can be assigned as $12H$-dibenzo[b, h]fluoren-12-one in analogy to coronene oxidation on preoxidized HOPG.[17] This species can be accessed in solution phase synthesis and was first prepared by R. Martin.[75] The dominant oxide $\mathbf{a_2^*}$ has no equivalent in the oxidation of any of the other PAHs studied here. Since the mass shifts with respect to pentacene are 4 u for ^{16}O and 6 u for ^{18}O, the stoichiometry has to be $C_{21}H_{22}O$. Our best guess is that an oxygen atom replaces a carbon atom forming an ether bond while a hydrogen atom gets transferred to another carbon atom. The most stable among such structures would be $14H$-dibenzo[a, j]xanthene (see fig. 9F) first prepared by solution phase synthesis as a byproduct of the reaction of β-naphthol with formamide by Saito et al.[76] Some other less likely structural candidates for $\mathbf{a_1^*}$ and $\mathbf{a_2^*}$ can be found in supplement.

Fullerene precursor $C_{60}H_{30}$, FPC

FPC has a three-fold symmetric, nonplanar structure (see fig. 2). Due to steric interaction between its three "rotor blades" it is slightly twisted. Therefore not all atoms in FPC adsorbates having their central hexagons oriented parallel to a flat substrate can be at the same distance to the surface. According to the DFT-calculated structure (for an isolated molecule without taking on-surface relaxation into account), the most "out-of-plane" hydrogen atom would be ca. 1 Å further away from the surface than the closest one.

As the TRMS map in fig. 10A reveals, multilayer oxidation again yields a series of epoxides **1-5**, which desorb at temperatures increasing from 580 K to 650 K corresponding to binding energies: in the range 2.0-2.2 eV.

On-top oxidation of FPC monolayers over a range of different O-atom doses does not yield any measurable desorption signal ($0\text{-}4.5 \cdot 10^{15}$ cm^{-2}). By contrast small amounts of lactones **b** are observed at small preoxidation oxygen loads (fig. 10B). Higher oxygen doses just deplete this signal, with only traces of the low-temperature component $\mathbf{a_2}$ remaining (fig. 10C).

Rubrene

As discussed in the background section, rubrene is a highly nonplanar PAH in which the armoatic systems of the central tetracene unit and the phenyl substituents are not conjugated. On HOPG, rubrene orients itself with the central tetracene unit parallel to the surface and arranges in a distorted, almost densely packed adsorbate structure.[77,78] Incomplete monolayers manifest a giraffe-skin-like film morphology when probed by AFM[53] (the "brown giraffe spots" being empty regions). Due to coverage dependent packing and orientation, ca. four times the ion dose required to form an HBC monolayer is needed to form a saturated rubrene monolayer. Correspondingly, a significant lateral intermolecular interaction energy of 42 meV has been measured.[53]

According to the TRMS map presented in fig. 11A, the oxidation of a rubrene multilayer film (8 ML) leads to an epoxide/ether series **1-7** (with traces of **8** or even **9**). Our DFT cal-
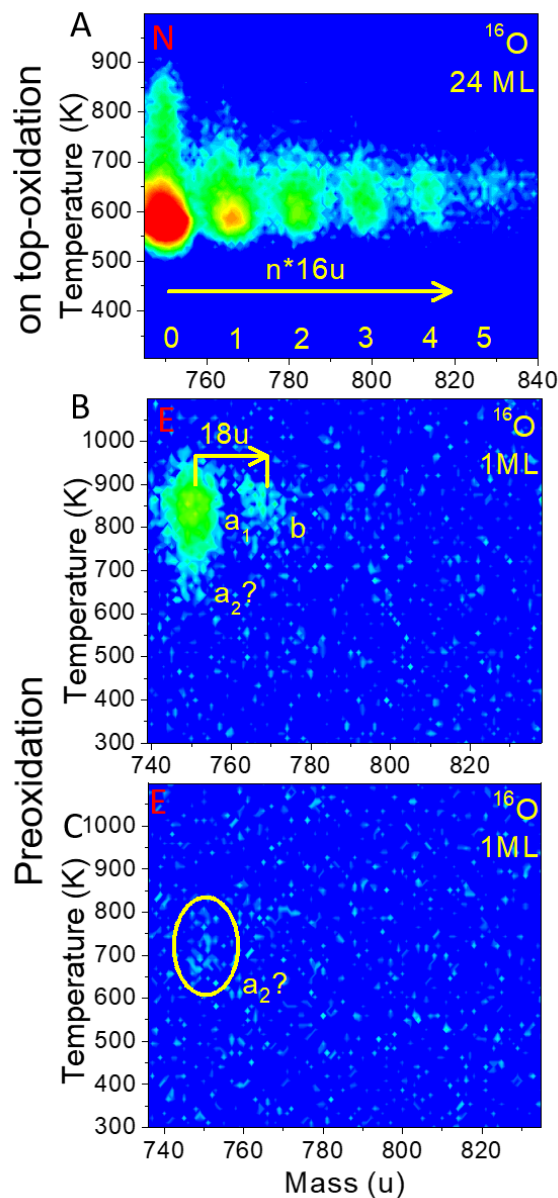
Figure 10: TRMS maps of FPC oxide films generated by A: TRMS map (NLIS) of on top-oxidation of 20 ML FPC with ^{16}O, D_O=4.5·10^{15} cm^{-2}, yielding epoxides **1-5**; TRMS map (ELIS) after depositing 1 ML FPC onto HOPG preoxidized with ^{16}O, D_O=3.6·10^{15} cm^{-2}, showing some lactones **b** ; D: TRMS map (ELIS) after the identical procedure as in (B) with D_O=1.8·10^{16} cm^{-2}; for all spectra β=4.3 K/s

culations (see supplement for details) indicate that it is energetically more favorable to add seven oxygen atoms to the tetracene backbone instead of oxidizing the phenyl rings. This is probably due to the aforementioned twisted nature of the tetracene unit. Observation of
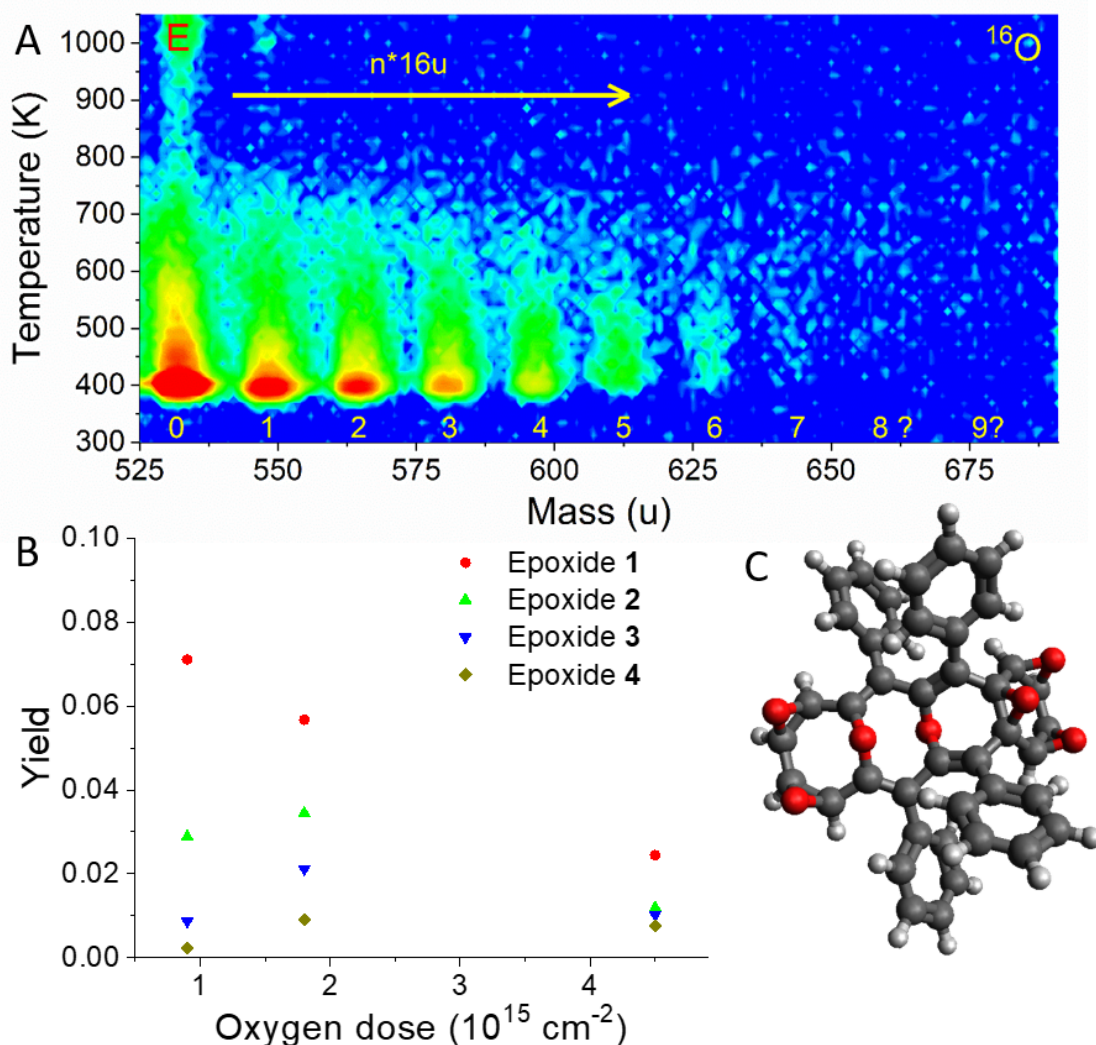
Figure 11: Rubrene multilayer oxidation experiments; A: TRMS map (ELIS) of 8 ML rubrene after oxidation with ^{16}O, $D_O=1.8 \cdot 10^{15}$ cm^{-2}, ELIS, $\beta=4.1$ K/s, showing a series of **0-9** adopted epoxy or ether functionalities at almost constant desorption temperatures; B: oxidation yields for the first epoxides as a function of the oxygen dose (rubrene redesorption always 0.4-0.45$\hat{\approx}$3.5 ML); C: most stable DFT structure for the seventh oxide ($C_{42}H_{28}O_7$) without destruction of the tetracene unit

such high oxygen loading implies a significant fraction of ethers. The overall oxide yields (see fig. 11B) start at 13% for low oxygen doses and decrease for higher doses. Among the three O-atom doses tried, best yields of higher epoxides were obtained for $1.8 \cdot 10^{15}$ cm^{-2}, the only dose for which we observed more than epoxide **4**. All epoxides/ethers n desorb at roughly the same temperature as the rubrene multilayer (ca. 400 K) so these oxides typically do not

come in contact with the HOPG surface before desorbing.

As outlined in fig. 12A+C, both monolayer procedures yield epoxides (or ethers) **1-3** (maybe
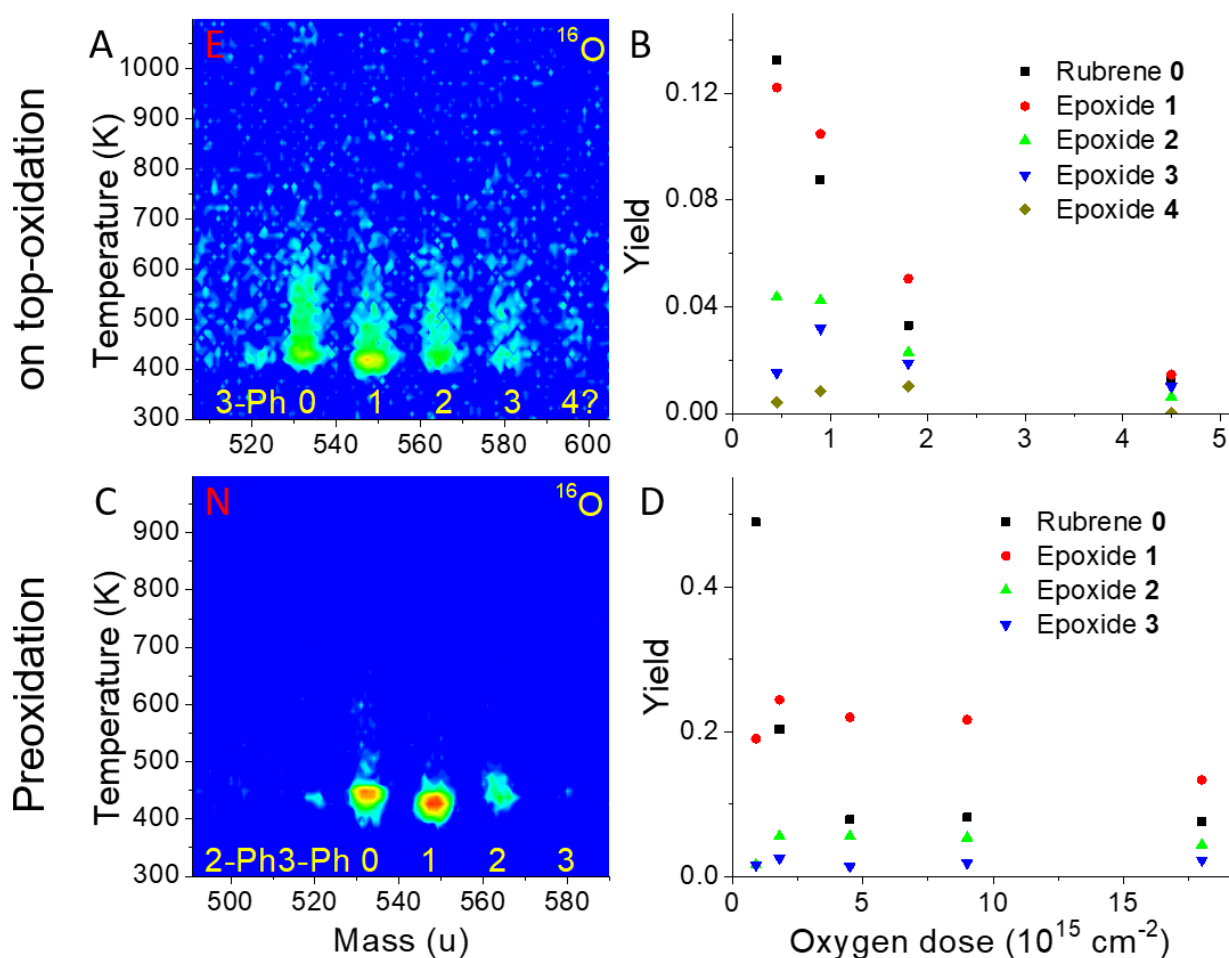

Figure 12: Rubrene monolayer oxidation; A: TRMS map (ELIS) showing the outcome of on-top oxidation of 0.5 ML rubrene with ^{16}O, $D_O=0.9\cdot10^{15}$ cm^{-2}, yielding epoxides **1-4**, exclusively; B: oxide yields for all species from (A) as a function of the oxygen dose; C: TRMS map (NLIS) of 0.5 ML rubrene deposited onto HOPG preoxidized with ^{16}O, $D_O=1.8\cdot10^{15}$ cm^{-2}, showing only epoxide **1-3** formation; D: oxide yields for all species from (C) as a function of the preoxidizing oxygen dose; for all spectra $\beta=4.1$ K/s

4 for on top-oxidation). Best yields are always achieved for very low oxygen doses.

Comparison of yields and mechanistic considerations

In the on-top oxidation of multilayer films, the overall oxide yields for the particular best oxygen dose were usually around 10% with the probed film thicknesses. In the case of

coronene[16] and HBC this corresponds to ca. 1.5 ML equivalents while for pentacene and rubrene it corresponds to 0.7 and 1.0 ML equivalents, respectively. This shows that the fully planar PAHs do not shield the lower layers from the impinging oxygen atoms completely since lower layers must have participated in the reaction. Since the redesorption signal of the non-planar PAHs is not equal to the initial coverage minus one layer, it is evident that the top layers do not shield lower layers from the atomic oxygen beam completely and that either non-desorbable products such as intermolecular ethers are formed or that a fraction of the formed oxides has decomposed before the desorption temperature has been reached. Especially for rubrene such competitive processes must play a major role since the signal of the unreacted species dropped down to 3.5 ML equivalents (44% of the initial 8 ML deposit) which indicates the highest oxygen penetration depth among the species investigated here. Except for HBC which for which the on-top oxidized monolayer behaved like the multilayer, the preoxidation sequence generated higher oxide yields than the monolayer on-top oxidation, often with a more diverse product distribution. The highest overall oxide yield was found for pentacene with 40% for best investigated dose followed by rubrene with ca. 30%. Coronene had desorbed with 10%[17] while for HBC and FPC both the absolute desorption intensity and the yields were rather low.

The low absolute desorption intensity of HBC and FPC is in part due to the simple fact that their monolayers consist of fewer molecules than for the other species in this work.[52,53] Another factor that probably decreases the oxide desorption is the desorption temperature: around 650 K, oxidized graphite begins to decompose under emission of CO and CO_2[16,19] which means that a large fraction of HBC and FPC oxides probably decompose before they can desorb. Furthermore, the "rotor" FPC structure is itself likely to be more sensitive to oxidative decomposition (to yield small volatiles which were not probed here) than the more compact PAHs due to its large open rim which causes the yield to be the lowest of all species in this work.

Pentacene shows a diverse surface oxidation chemistry which differs significantly from coronene,

HBC and FPC. There are several factors that may contribute to this: pentacene has only one Clar sextet which is an indicator for a higher reactivity in comparison with the other species. Also, all of its hexagons are arranged in a linear annulated chain, i.e. there are no core carbon atoms. As a result, deformations of the carbon framework are easier than for the much more rigid disc-like PAHs coronene or HBC and new types of oxide products can be accessed.

For rubrene, no "special oxides" such as lactones or quinones were observed. There are two possible explanations: (a) epoxide formation is somehow kinetically favored over other types of oxide or more likely (b) the perpendicularly oriented phenyl substituents cause the tetracene backbone to be too far away from the surface to be able to participate in surface-catalytic or surface-mediated reactions.

In our previous work on coronene oxidation we have argued that the difference in species desorbed from oxidized multilayers versus monolayers shows that the surface participates significantly in monolayer oxidation. We in fact used the observation of coronene lactone formation in the case of monolayers to infer (i) mobile oxygen atoms on the graphite basal plane and (ii) transfer of one or more O-atoms from the surface to adsorbed PAHs during the oxidation process. The mobility of O atoms has been further investigated in a recent theoretical study by Zhang et al.[79] showing good agreement with the considerations made in our own studies on coronene oxidation.[17] In the present study, we have been able to confirm strong differences between monolayer and multilayer oxidation for all PAHs studied with the exception of the on-top oxidized HBC monolayers and rubrene for which the distance between surface and reactive tetracene backbone appears to be too large to allow efficient O-atom transfer. Additionally, in the case of pentacene we were able for the first time to directly confirm uptake of an epoxy functionality from the preoxidized HOPG surface because it leads to a unique reaction product not observed by on-top oxidation.

Thus we have obtained further evidence for surface mediated oxidation of PAHs when subjected to our reaction conditions. Whether this already occurs during room temperature

exposure to reactive O-atoms or is thermally activated during the desorption ramp remains unclear. We note however, that certain pentacene oxides (**0c2**) are already observed to desorb from a preoxidized surface below 400 K which puts an upper limit on the temperature required for the corresponding reaction to occur.

Conclusion

We have used TPD to compare the reactivity of five different PAHs (coronene, HBC, pentacene, FPC and rubrene) with (i) near thermal energy effusive beams of atomic oxygen perpendicularly incident from gas-phase onto PAH films or alternatively (ii) with preoxidized graphite surfaces onto which PAHs were subsequently deposited. Thick films of all PAHs take up atomic oxygen to form intactly desorbable epoxides or, for higher oxygen doses also ethers. By contrast, deposition of PAHs onto graphite surface (ep)oxides leads to different products indicative of surface-mediated oxidation. The fully planar PAHs coronene and HBC form lactones, while the "linear" pentacene preferentially forms quinones. Despite being non-planar, FPC also forms lactones and can therefore still be classified as nanographene-like with regard to its monolayer oxidation reactivity. Rubrene deviates most strongly from the typical nanographene reactivity pattern: the central (reactive) tetracene backbone is too far away for surface mediated oxidation.

Depending on the PAH, the maximum observed number of adopted oxygen atoms was **5-7**, i.e. on the order of one O-atom per hexagon. Furthermore, we have observed, that the flux of subliming oxides decays with an increasing number of adopted oxygen atoms (in particular for thick planar PAH films). Given that O-atom doses were varied over a range which should have led to higher observed adoption numbers for unit sticking and fragmentation-free sublimation, this implies a pronounced destabilization of the heavy oxides preventing their escape as intact molecules during heating by forming small volatile fragments and interlinking to generate non-desorbable carbonaceous phases.

From a more applied point of view, we have shown that heterogeneous oxidation of PAHs with atomic oxygen can be used to generate a homologous series of size- and composition controlled oxides ranging in size up to $C_{60}H_{30}O_5$. Scale-up, e.g. by adsorbing, oxidizing and desorbing simultaneously is conceivable. Most of these species are efficiently sublimable such that selective, T-controlled transfer to clean electrically insulating surfaces under UHV conditions is feasible. This would allow spectroscopic probes, e.g. of photoluminescence, which may in turn be of interest for nanotechnological applications.[4]

Acknowledgement

Supporting Information Available

The supplementary material contains:

- the results of benchmark experiments for pentacene with low electron impact energy

- further TRMS maps for HBC and pentacene acquired after oxidation with different oxygen isotopes

- all DFT calculated molecular structures with relative stabilities

References

(1) Müllen, K.; Rabe, J. P. Nanographenes as Active Components of Single-Molecule Electronics and How a Scanning Tunneling Microscope Puts Them To Work. *Acc. Chem. Res.* **2008**, *41*, 511–520.

(2) Zhou, X.; Yu, G. Modified Engineering of Graphene Nanoribbons Prepared via On-Surface Synthesis. *Adv. Mater.* **2020**, *32*, 1905957.

(3) Shang, J.; Ma, L.; Li, J.; Ai, W.; Yu, T.; Gurzadyan, G. G. The Origin of Fluorescence from Graphene Oxide. *Sci. Rep.* **2012**, *2*, 792.

(4) Huang, X.-M.; Liu, L.-Z.; Zhou, S.; Zhao, J.-J. Physical properties and device applications of graphene oxide. *Front. Phys.* **2020**, *15*, 33301.

(5) Hummers, W. S.; Offeman, R. E. Preparation of Graphitic Oxide. *J. Am. Chem. Soc.* **1958**, *80*, 1339–1339.

(6) Staudenmaier, L. Verfahren zur Darstellung der Graphitsäure. *Ber. dt. chem. Ges.* **1898**, *31*, 1481–1487.

(7) He, H.; Riedl, T.; Lerf, A.; Klinowski, J. Solid-State NMR Studies of the Structure of Graphite Oxide. *J. Phys. Chem.* **1996**, *100*, 19954–19958.

(8) Porro, S.; Accornero, E.; Pirri, C. F.; Ricciardi, C. Memristive Devices Based on Graphene Oxide. *Carbon* **2015**, *85*, 383 – 396.

(9) Eda, G.; Lin, Y.-Y.; Miller, S.; Chen, C.-W.; Su, W.-F.; Chhowalla, M. Transparent and Conducting Electrodes for Organic Electronics from Reduced Graphene Oxide. *Appl. Phys. Lett.* **2008**, *92*, 233305.

(10) Porro, S.; Ricciardi, C. Memristive Behaviour in Inkjet Printed Graphene Oxide Thin Layers. *RSC Adv.* **2015**, *5*, 68565–68570.

(11) Wang, L.-H.; Yang, W.; Sun, Q.-Q.; Zhou, P.; Lu, H.-L.; Ding, S.-J.; Wei Zhang, D. The Mechanism of the Asymmetric SET and RESET Speed of Graphene Oxide Based Flexible Resistive Switching Memories. *Appl. Phys. Lett.* **2012**, *100*, 063509.

(12) Wang, X.; Tian, H.; Mohammad, M. A.; Li, C.; Wu, C.; Yang, Y.; Ren, T.-L. A Spectrally Tunable all-Graphene-Based Flexible Field-Effect Light-Emitting Device. *Nature Commun.* **2015**, *6*, 7767.

(13) Gorreta, S.; Pons-Nin, J.; López, G.; Figueras, E.; Jové-Casulleras, R.; Araguz, C.; Via, P.; Camps, A.; Domínguez-Pumar, M. A CubeSAT payload for in-situ monitoring of pentacene degradation due to atomic oxygen etching in LEO. *Acta Astronaut.* **2016**, *126*, 456 – 462.

(14) Whittet, D. C. B. Oxygen Depletion in the Interstellar Medium: Implications for Grain Models and the Distribution of Elemental Oxygen. *Astrophys. J.* **2010**, *710*, 1009–1016.

(15) Vollmer, A.; Weiss, H.; Rentenberger, S.; Salzmann, I.; Rabe, J.; Koch, N. The Interaction of Oxygen and Ozone with Pentacene. *Surf. Sci.* **2006**, *600*, 4004 – 4007.

(16) Weippert, J.; Ulas, S.; Strelnikov, D.; Böttcher, A.; Kappes, M. M. Formation of Sublimable Nanographene Oxides by Reacting Coronene Films with Atomic Oxygen. *J. Phys. Chem. C* **2018**, *122*, 28588–28600.

(17) Weippert, J.; Gewiese, V.; Böttcher, A.; Kappes, M. M. Graphite-Mediated Oxidation of Coronene Adsorbates: A UHV Study. *J. Phys. Chem. C* **2018**, *122*, 28601–28612.

(18) Barinov, A.; Malcioglu, O. B.; Fabris, S.; Sun, T.; Gregoratti, L.; Dalmiglio, M.; Kiskinova, M. Initial Stages of Oxidation on Graphitic Surfaces: Photoemission Study and Density Functional Theory Calculations. *J. Phys. Chem. C* **2009**, *113*, 9009–9013.

(19) Larciprete, R.; Lacovig, P.; Gardonio, S.; Baraldi, A.; Lizzit, S. Atomic Oxygen on

Graphite: Chemical Characterization and Thermal Reduction. *J. Phys. Chem. C* **2012**, *116*, 9900–9908.

(20) Li, J.-L.; Kudin, K. N.; McAllister, M. J.; Prud'homme, R. K.; Aksay, I. A.; Car, R. Oxygen-Driven Unzipping of Graphitic Materials. *Phys. Rev. Lett.* **2006**, *96*, 176101.

(21) Gu, Q.; Wen, G.; Ding, Y.; Wu, K.-H.; Chen, C.; Su, D. Reduced Graphene Oxide: a Metal-Free Catalyst for Aerobic Oxidative Desulfurization. *Green Chem.* **2017**, *19*, 1175–1181.

(22) Zhao, Z.; Dai, Y.; Ge, G.; Wang, G. Efficient Tuning of Microstructure and Surface Chemistry of Nanocarbon Catalysts for Ethylbenzene Direct Dehydrogenation. *AIChE J. 61*, 2543–2561.

(23) Li, Y.-F.; Guo, M.-Q.; Yin, S.-F.; Chen, L.; Zhou, Y.-B.; Qiu, R.-H.; Au, C.-T. Graphite as a Highly Efficient and Stable Catalyst for the Production of Lactones. *Carbon* **2013**, *55*, 269 – 275.

(24) Scott, L. T. Methods for the Chemical Synthesis of Fullerenes. *Angew. Chem. Int. Ed. 43*, 4994–5007.

(25) Watson, M. D.; Fechtenkötter, A.; Müllen, K. Big Is Beautiful - Aromaticity Revisited from the Viewpoint of Macromolecular and Supramolecular Benzene Chemistry. *Chem. Rev.* **2001**, *101*, 1267–1300.

(26) Solà, M. Forty Years of Clar's Aromatic π-Sextet Rule. *Front. Chem.* **2013**, *1*, 22.

(27) Clar, E.; Zander, M. Aromatische Kohlenwasserstoffe, LXXII. Mitteil. : Die Zusammen-hänge zwischen chemischer Reaktivität, Phosphorescenz und para-Absorptionsbanden und die Wasserstoffähnlichkeit" des oberen Niveaus der p-Banden in den Absorption-sspektren aromatischer Kohlenwasserstoffe. *Chem. Ber.* **1956**, *89*, 749–762.

(28) Clar, E. The Building Principles of Aromatic Hydrocarbons. *J. Synth. Org. Chem Jpn.* **1962**, *20*, 862–865.

(29) Schroeder, P. G.; France, C. B.; Parkinson, B. A.; Schlaf, R. Orbital Alignment at p-Sexiphenyl and Coronene/Layered Materials Interfaces Measured with Photoemission Spectroscopy. *J. Appl. Phys.* **2002**, *91*, 9095–9107.

(30) Hendel, W.; Khan, Z.; Schmidt, W. Hexa-peri-benzocoronene, a Candidate for the Origin of the Diffuse Interstellar Visible Absorption Bands? *Tetrahedron* **1986**, *42*, 1127–1134.

(31) Sánchez-Sánchez, C.; Martínez, J. I.; Lanzilotto, V.; Biddau, G.; Gómez-Lor, B.; Pérez, R.; Floreano, L.; López, M. F.; Martín-Gago, J. A. Chemistry and Temperature-Assisted Dehydrogenation of $C_{60}H_{30}$ Molecules on $TiO_2(110)$ Surfaces. *Nanoscale* **2013**, *5*, 11058–11065.

(32) Schroeder, P. G.; France, C. B.; Park, J. B.; Parkinson, B. A. Orbital Alignment and Morphology of Pentacene Deposited on Au(111) and SnS_2 Studied Using Photoemission Spectroscopy. *J. Phys. Chem. B* **2003**, *107*, 2253–2261.

(33) Tuğluoğlu, N.; Baris, B.; Gürel, H.; Karadeniz, S.; Yüksel, O. F. Investigation of Optical Band Gap and Device Parameters of Rubrene Thin Film Prepared Using Spin Coating Technique. *J. Alloys Compd.* **2014**, *582*, 696–702.

(34) Rieger, R.; Kastler, M.; Enkelmann, V.; Müllen, K. Entry to Coronene Chemistry - Making Large Electron Donors and Acceptors. *Chem. Eur. J.* **2008**, *14*, 6322–6325.

(35) Zinke, A.; Ott, R.; Sobotka, M. Zur Kenntnis des Coronens II. Kurze Mitteilung: Über ein Coronenchinon-1,2. *Monatsh. Chem.* **1952**, *83*, 546–548.

(36) Alibert-Fouet, S.; Seguy, I.; Bobo, J.-F.; Destruel, P.; Bock, H. Liquid-Crystalline and

Electron-Deficient Coronene Oligocarboxylic Esters and Imides By Twofold Benzogenic Diels–Alder Reactions on Perylenes. *Chem. Eur. J.* **2007**, *13*, 1746–1753.

(37) Rieger, R.; Kastler, M.; Enkelmann, V.; Müllen, K. Entry to Coronene Chemistry—Making Large Electron Donors and Acceptors. *Chem. Eur. J.* **2008**, *14*, 6322–6325.

(38) Rohr, U.; Schlichting, P.; Böhm, A.; Gross, M.; Meerholz, K.; Bräuchle, C.; Müllen, K. Liquid Crystalline Coronene Derivatives with Extraordinary Fluorescence Properties. *Angew. Chem. Int. Ed.* **1998**, *37*, 1434–1437.

(39) Yamada, H.; Yamashita, Y.; Kikuchi, M.; Watanabe, H.; Okujima, T.; Uno, H.; Ogawa, T.; Ohara, K.; Ono, N. Photochemical Synthesis of Pentacene and its Derivatives. *Chem. Eur. J.* **2005**, *11*, 6212–6220.

(40) Kytka, M.; Gerlach, A.; Schreiber, F.; Kovac, J. Real-time Observation of Oxidation and Photo-Oxidation of Rubrene Thin Films by Spectroscopic Ellipsometry. *Appl. Phys. Lett.* **2007**, *90*, 131911.

(41) Sinha, S.; Wang, C.-H.; Mukherjee, M.; Mukherjee, T.; Yang, Y.-W. Oxidation of Rubrene Thin Films: An Electronic Structure Study. *Langmuir* **2014**, *30*, 15433–15441.

(42) Wadumethrige, S. H.; Rathore, R. A Facile Synthesis of Elusive Alkoxy-Substituted Hexa-peri-hexabenzocoronene. *Org. Lett.* **2008**, *10*, 5139–5142.

(43) Clar, E.; John, F. Zur Kenntnis mehrkerniger aromatischer Kohlenwasserstoffe und ihrer Abkömmlinge, V. Mitteil.: Naphtho-anthracene, ihre Oxydationsprodukte und eine neue Klasse tiefgefärbter Kohlenwasserstoffe. *Ber. dt. chem. Ges.* **1929**, *62*, 3021–3029.

(44) Ried, W.; Anthöfer, F. Einfache Synthese für Pentacen-6,13-chinon. *Angew. Chem. 65*, 601.

(45) Pandit, V. U.; Arbuj, S. S.; Mulik, U. P.; Kale, B. B. Novel Functionality of Organic 6,13-Pentacenequinone as a Photocatalyst for Hydrogen Production under Solar Light. *Environ. Sci. Technol.* **2014**, *48*, 4178–4183.

(46) Lee, S.-L.; Lin, C.-H.; Cheng, K.-Y.; Chen, Y.-C.; Chen, C.-h. Stability of Guest-Incorporated 2D Molecular Networks. *J. Phys. Chem. C* **2016**, *120*, 25505–25510.

(47) Lin, Y.; Wu, K.-H.; Lu, Q.; Gu, Q.; Zhang, L.; Zhang, B.; Su, D.; Plodinec, M.; Schlögl, R.; Heumann, S. Electrocatalytic Water Oxidation at Quinone-on-Carbon: A Model System Study. *J. Am. Chem. Soc.* **2018**, *140*, 14717–14724.

(48) Pandit, V.; Arbuj, S.; Hawaldar, R.; Kshirsagar, P.; Mulik, U.; Gosavi, S.; Park, C.-J.; Kale, B. In Situ Preparation of a Novel Organo-Inorganic 6,13-Pentacenequinone–TiO_2 Coupled Semiconductor Nanosystem: a New Visible Light Active Photocatalyst for Hydrogen Generation. *J. Mater. Chem. A* **2015**, *3*, 4338–4344.

(49) Käfer, D.; Witte, G. Growth of Crystalline Rubrene Films with Enhanced Stability. *Phys. Chem. Chem. Phys.* **2005**, *7*, 2850–2853.

(50) Liu, R.; Wu, D.; Feng, X.; Müllen, K. Bottom-Up Fabrication of Photoluminescent Graphene Quantum Dots with Uniform Morphology. *J. Am. Chem. Soc.* **2011**, *133*, 15221–15223.

(51) Kabdulov, M.; Jansen, M.; Amsharov, K. Y. Bottom-Up C_{60} Fullerene Construction from a Fluorinated $C_{60}H_{21}F_9$ Precursor by Laser-Induced Tandem Cyclization. *Chem. Eur. J.* **2013**, *19*, 17262–17266.

(52) Weippert, J.; Hauns, J.; Bachmann, J.; Böttcher, A.; Yao, X.; Yang, B.; Narita, A.; Müllen, K.; Kappes, M. M. A TPD-based determination of the graphite interlayer cohesion energy. *J. Chem. Phys.* **2018**, *149*, 194701.

(53) Weippert, J.; Huber, P.; Schulz, A.; Amsharov, K. Y.; Böttcher, A.; Kappes, M. M. Influence of Dispersion Interactions on the Thermal Desorption of Nonplanar Polycyclic Aromatic Hydrocarbons on HOPG. *Phys. status solidi RRL* **2019**, *13*, 1900348.

(54) Anton, R.; Wiegner, T.; Naumann, W.; Liebmann, M.; Klein, C.; Bradley, C. Design and Performance of a Versatile, Cost-Effective Microwave Electron Cyclotron Resonance Plasma Source for Surface and Thin Film Processing. *Rev. Sci. Inst.* **2000**, *71*, 1177–1180.

(55) Gudmundsson, J. T. Recombination and Detachment in Oxygen Discharges: the Role of Metastable Oxygen Molecules. *J. Phys. D: Appl. Phys.* **2004**, *37*, 2073–2081.

(56) Ionin, A. A.; Kochetov, I. V.; Napartovich, A. P.; Yuryshev, N. N. Physics and Engineering of Singlet Delta Oxygen Production in Low-Temperature Plasma. *J. Phys. D: Appl. Phys.* **2007**, *40*, R25–R61.

(57) Redhead, P. Thermal Desorption of Gases. *Vacuum* **1962**, *12*, 203 – 211.

(58) Falconer, J.; Madix, R. Flash Desorption Activation Energies: DCOOH Decomposition and CO Desorption from Ni (110). *Surf. Sci.* **1975**, *48*, 393 – 405.

(59) TURBOMOLE V7.4.1 2019, a development of University of Karlsruhe and-Forschungszentrum Karlsruhe GmbH, 1989-2007,TURBOMOLE GmbH, since 2007; available from
http://www.turbomole.com.

(60) Balasubramani, S. G.; Chen, G. P.; Coriani, S.; Diedenhofen, M.; Frank, M. S.; Franzke, Y. J.; Furche, F.; Grotjahn, R.; Harding, M. E.; Hättig, C. et al. TURBO-MOLE: Modular program suite for ab initio quantum-chemical and condensed-matter simulations. *J. Chem. Phys.* **2020**, *152*, 184107.

(61) Becke, A. Density-Functional Exchange Energy Approximation with Correct Asymptotic Behaviour. *Phys. Rev. A* **1988**, *38*, 3098–3100.

(62) Perdew, J. Density-Functional Approximation for the Correlation-Energy of the Inhomogenous Electron Gas. *Phys. Rev. B* **1986**, *33*, 8822–8824.

(63) Schäfer, A.; Horn, H.; Ahlrichs, R. Fully Optimized Contracted Gaussian Basis Sets for Atoms Li to Kr. *J. Chem. Phys.* **1992**, *97*, 2571–2577.

(64) Eichkorn, K.; Treutler, O.; Öhm, H.; Häser, M.; Ahlrichs, R. Auxiliary Basis Sets to Approximate Coulomb Potentials. *Chem. Phys. Lett.* **1995**, *240*, 283 – 290.

(65) Deglmann, P.; Treutler, O.; Öhm, H.; Häser, M.; Ahlrichs, R. Nuclear Second Analytical Derivative Calculations Using Auxiliary Basis Set Expansions. *Chem. Phys. Lett.* **1995**, *384*, 103–107.

(66) Vosko, S.; Wilk, L.; Nusair, M. Accurate Spin-Dependent Electron Liquid Correlation Energies for Local Spin Density Calculations: a Critical Analysis. *Can. J. Phys.* **1980**, *58*, 1200–1211.

(67) Lee, C.; Yang, W.; Parr, R. Development of the Colle-Salvetti Correlation-Energy Formula into a Functional of the Electron Density. *Phys. Rev. B* **1988**, *37*, 785–789.

(68) Becke, A. Density-Functional Thermochemistry III The Role of Exact Exchange. *J. Chem. Phys.* **1993**, *98*, 5648–5652.

(69) Weigend, F.; Häser, M.; Patzelt, H.; Ahlrichs, R. RI-MP2: Optimized Auxiliary Basis Sets and Demonstration of Efficiency. *Chem. Phys. Lett.* **1998**, *294*, 143–152.

(70) Eichkorn, K.; Weigend, F.; Treutler, O.; Ahlrichs, R. Auxiliary Basis Sets for Main Row Atoms and Transition Metals and their Use to Approximate Coulomb Potentials. *Theor. Chem. Acc.* **1997**, *97*, 119–124.

(71) Grimme, S.; Antony, J.; Ehrlich, S.; Krieg, H. A Consistent and Accurate Ab Initio Parametrization of Density Functional Dispersion Correction (DFT-D) for the 94 Elements H-Pu. *J. Chem. Phys.* **2010**, *132*, 154104.

(72) Klues, M.; Witte, G. Crystalline Packing in Pentacene-like Organic Semiconductors. *CrystEngComm* **2018**, *20*, 63–74.

(73) Chen, W.; Huang, H.; Thye, A.; Wee, S. Molecular Orientation Transition of Organic Thin Films on Graphite: the Effect of Intermolecular Electrostatic and Interfacial Dispersion Forces. *Chem. Commun.* **2008**, *36*, 4276–4278.

(74) Götzen, J.; Käfer, D.; Wöll, C.; Witte, G. Growth and Structure of Pentacene Films on Graphite: Weak Adhesion as a Key for Epitaxial Film Growth. *Phys. Rev. B* **2010**, *81*, 085440.

(75) Martin, R. H. 125. Polycyclic Aromatic Hydrocarbons. Part XXVIII. Dibenzfluorenes. *J. Chem. Soc.* **1941**, 679–685.

(76) Saito, N.; Tanaka, C.; Okubo, M. Studies on the Reactions of Formamide. I. *Pharm. Soc. Jpn.* **1956**, *76*, 359–361.

(77) Ueba, T.; Park, J.; Terawaki, R.; Watanabe, Y.; Yamada, T.; Munakata, T. Unoccupied Electronic Structure and Molecular Orientation of Rubrene; from Evaporated Films to Single Crystals. *Surf. Sci.* **2016**, *649*, 7 – 13.

(78) Udhardt, C.; Forker, R.; Gruenewald, M.; Watanabe, Y.; Yamada, T.; Ueba, T.; Munakata, T.; Fritz, T. Optical Observation of Different Conformational Isomers in Rubrene Ultra-Thin Molecular Films on Epitaxial Graphene. *Thin Solid Films* **2016**, *598*, 271 – 275.

(79) Zhang, Q.; Li, Y.; Cao, Z. Oxygen Migration and Optical Properties of the Coronene

Oxides and their Persulfurated Derivatives: Insight into the Electric Field Effect and the Oxygen-Site Dependence. *Phys. Chem. Chem. Phys.* **2020**, *22*, 20078–20086.
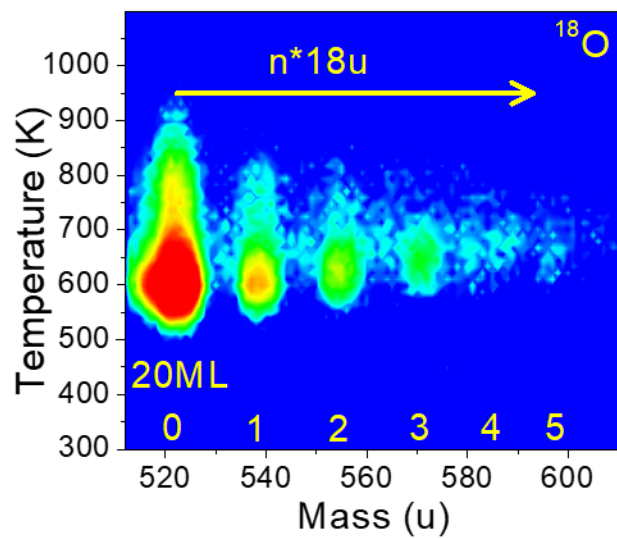

Figure 13: TOC graphic